Journal of
Marine Science and Engineering

MDPI

Article

Wind-Wave Characterization in a Wind-Jet Region: The Ebro Delta Case

Laura Ràfols [1,2,*], Elena Pallares [1], Manuel Espino [1], Manel Grifoll [1], Agustín Sánchez-Arcilla [1], Manel Bravo [2] and Abdel Sairouní [2]

1 Laboratori d'Enginyeria Marítima, Universitat Politècnica de Catalunya - BarcelonaTech (UPC), C/Jordi Girona 1-3 Edif. D1, 08034 Barcelona, Spain; elena.pallares@upc.edu (E.P.); manuel.espino@upc.edu (M.E.); manel.grifoll@upc.edu (M.G.); agustin.arcilla@upc.edu (A.S.-A.)

2 Servei Meteorològic de Catalunya (SMC), C/Berlin 38-48 4a, 08029 Barcelona, Spain; mbravob@meteo.cat (M.B.); asairouni@meteo.cat (A.S.)

* Correspondence: laura.rafols@upc.edu; Tel.: +34-93-405-4631

Academic Editors: Harshinie Karunarathna and Jenifer Brown
Received: 15 October 2016; Accepted: 14 February 2017; Published: 20 February 2017

Abstract: This manuscript describes the wind-wave generation, development and fading in a complex area: a wind-jet region. The study region is the offshore Ebro Delta (NW Mediterranean Sea) where strong cross-shelf winds occur due to a topographic channelization. This leads to relatively short-fetch conditions, which interact with the swell component. The third-generation wave model Simulating WAves Nearshore (SWAN) is implemented and fed by high-resolution wind fields. A combination of buoy and High Frequency (HF) radar data is used for model validation, resulting in a reasonable level of agreement. The numerical results characterize the wind-wave evolution during a wind jet. A bimodal spectrum is observed due to the interaction of swell and sea systems. The wave directional spreading exhibits lower values at the wind-jet axis. Finally, a reliability analysis of the wave data from an HF radar deployed at the region is carried out.

Keywords: waves; bimodal spectra; directional spreading; HF radar; Ebro Delta

1. Introduction

In spite of its limited fetch, the NW Mediterranean Sea is able to generate harmful storms. The prediction of such storms near the coast is a difficult challenge for operational oceanography and risk management due to wind interaction with local topography, sharply-varying fields, the resulting sea-swell interaction and the influence of the land-sea border [1]. These difficulties are especially true during coastal wind-jet episodes.

In this sense, coastal wind-jet regions are areas with highly complex dynamics due to the occurrence of strong gradients in the wind field and the interaction with local (sea) and remote (swell) wave conditions. The investigation of wave evolution in wind-jet areas is relatively scarce. For instance, [2] investigated the fetch-limited wind-wave development under alternating coastal wind jets and wakes in the Pacific coast of northern Japan. The study in [3] investigated the wind-waves in the Red Sea, where different mountain gap wind jets occur and induce an enhancement of wave heights.

The knowledge of wave directional characteristics and energy distribution is of high importance due to its application to marine structure design, coastal engineering, coastal vulnerability assessment and coastal protection (e.g., implementation of an early warning system). In this sense, [4] studied the effect of fetch on the directional spectrum of the Celtic Sea storm waves using measurements from a high-frequency radar. The work in [5] investigated the variability of wave directions during sea storms and found that it is large for lower sea states (storm tail) and is reduced for storm peaks.

Wave modeling is a very useful tool to analyze the spatial evolution of the wave directional response. In this regard, [6] used the WAVEWATCH-III wave model to analyze the sea-surface directional wave spectrum under typhoon wind forcing in the South China Sea. And [7] used the Simulating WAves Nearshore (SWAN) wave model to study the wave spectral response to sudden changes in wind direction in finite-depth waters. They found that in a 180° wind turn, the young wind-sea decouples from the old waves, and a bimodal spectrum is observed. In contrast, in a 90° wind turn, the spectrum is rotated smoothly to the new direction and remains unimodal.

The Ebro Delta (NW Mediterranean Sea) is a region where wind jets develop from topographic conditions. The works in [8] and [9] highlighted the strong gradients in wind and wave fields in this region. There are many studies focused on this area, which characterize the wave climate ([1,10]), analyze the wave growth ([8,11]) and evaluate the wind-wave response during energetic events ([9,12]). However, there is not an exhaustive investigation of the wind-wave directional response and its temporal and spatial evolution during a wind jet. For this reason, the purpose of this study is to analyze the directional wave properties in order to characterize the fetch-limited wind-wave development during intense wind jets at the Ebro Delta. With this aim, a state-of-the-art numerical wave model has been implemented and run for two months (from March 15 2014 to May 15 2014). This period was selected due to observational data availability and the occurrence of several wind-jet events. A skill assessment of the model is carried out with the available dataset, and the usefulness of the wave data from an HF radar deployed at the region is evaluated.

This study is organized as follows. In Section 2, the main characteristics of the study area are presented, as well as the used observational data and the implemented numerical model. The results are described in Section 3, including an examination of the wind field, a validation of the numerical model and a detailed analysis of a wind-jet event. Then, a discussion is presented in Section 4, which also includes an investigation of the reliability of the Ebro Delta HF radar. Finally, the main conclusions are summarized in Section 5.

2. Experimental Section

2.1. Study Area

The Ebro Delta is located at the southern part of the Catalan coast, between latitudes 40.4°–41.1° N and longitudes 0.4°–1.3° E (see Figure 1). The most characteristic wind of the region is the northwesterly wind (mistral), which is channeled through the Ebro Valley resulting in intensified wind when it reaches the sea. This wind jet is dry, cold, perpendicular to the coastline and associated with high wind intensities. It is more usual and intense in autumn and winter [13], when a larger atmospheric pressure gradient takes place, but a small pressure difference along the Ebro Valley is enough to initiate wind during any season [14].

The NW Mediterranean coast has particular features that create a relatively complex wave climate ([10]): complex bathymetry, short fetches, short wave storm durations and high wind field variability in time and space. Particularly, at the Ebro Delta, the wave climate is characterized by a predominance of NW conditions (which coincides with the predominance of NW winds) with also significant E and S storms. These storms tend to develop a bimodal directional spectrum due to the coexistence of sea and swell waves ([10]). The work in [1] found that, during eastern and southern storms, swell dominates (60%), while for NW storms (offshore winds), the sea system dominated (96%). Although there are more deltas along the Catalan coast, the Ebro Delta is the one that shows a greater presence of wave bimodal spectra.

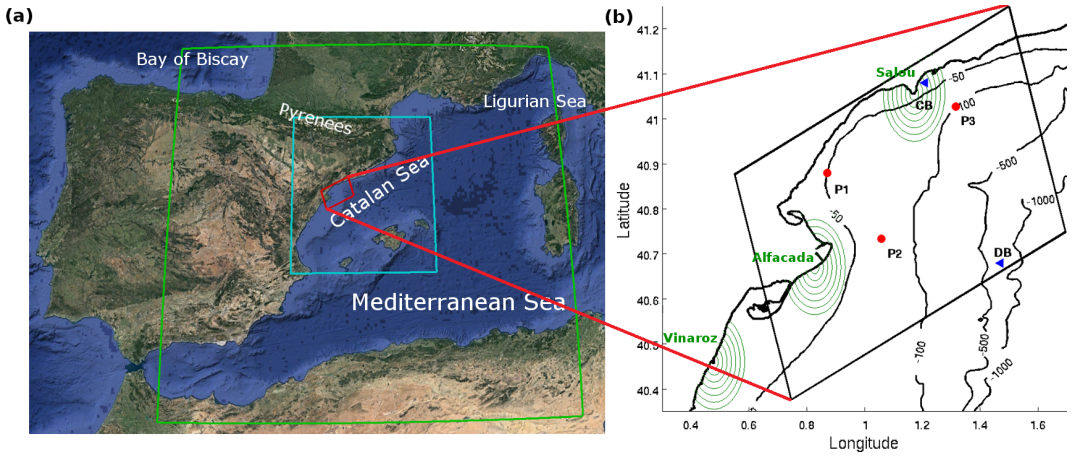

Figure 1. (**a**) Geographical location of the Ebro Delta in the NW Mediterranean Sea. Green, blue and red boxes show the three nested numerical domains used in this study. (**b**) Local domain at the Ebro Delta with the HF radar range arcs (in green), the buoy locations (blue triangles) and the location of three points used for analysis (in red: P1, P2 and P3).

2.2. Observations

For validation purposes, oceanographic and coastal meteorological measurements from the Spanish Harbour Agency (Puertos del Estado, http://www.puertos.es) are used. Specifically, data were obtained from a coastal Wave Buoy (CB), a Deep Water Buoy (DB) and an HF radar (see Figure 1). The deep water buoy was deployed in August 2004 and is an ocean Seawatch buoy located at 40.6° N, 1.47° E at a 688-m depth. The coastal wave buoy is a Triaxys buoy located at 41.07° N, 1.19° E at a 15-m depth, deployed in November 1992. Both buoys provide significant wave height, peak period, nautical direction and directional spectra, among other data (the technical characteristics of both buoys are available at www.puertos.es). Additionally, the DB also provides wind intensity and direction data. The spectrum of each buoy is calculated in a different way. DB provides the energy spectrum divided into 14 bands, and each band has a fixed fraction of energy. This way, it does not measure in a fixed frequency range, because it depends on the amount of energy measured. In contrast, CB calculates a scalar spectrum doing an average of 128 points with a sampling frequency of 1.28 Hz, which corresponds to a Δf of 0.01 Hz. The measured frequency range goes from 0.03 Hz to 0.66 Hz.

The HF radar system used in this study is a CODAR SeaSonde standard-range system composed of three remote shelf-based sites (Salou, Alfacada and Vinaroz; see locations in Figure 1) that operate at 13.5 MHz. Each site provides measurements of wave height, central period and direction along seven concentric arcs (plotted in green in Figure 1) every 30 min, with the most offshore arc situated 11.6 km from the antenna. In contrast to HF radar current measurements, which are obtained from the first-order peaks in the radar echo spectrum, the HF radar wave data are derived from the second-order radar spectrum ([15]). The method used to derive the data are based on a least-squares fitting of the radar spectrum with the Pierson–Moskowitz model for the ocean wave spectrum. It assumes that the ocean wave spectrum is homogeneous over the range cell. For this reason, the smaller close-in radar range cells are used for wave analysis ([15]). It is important to note that measured waves are limited to those felt by the Bragg waves, so the shortest wave period included in the HF radar data is 5 s ([16]).

In order to evaluate the HF radar performance, two scatter plots comparing the HF radar data and the measurements at CB are presented in Figure 2. The first one (Figure 2a) was undertaken with the entire available data period (seven months) and the second one (two months) with the data corresponding to the study period of this study, which has been selected due to the presence of four NW wind-jet events. The HF radar data used in these comparisons belongs to the data measured at

the third arc of the Salou antenna, which is the closest to CB (see Figure 1). In order to avoid isolated data points and inconsistent values, the HF radar data have been filtered (see Section 3.2). Both scatter plots present good agreement between the HF radar data and the CB measurements. However, the HF radar tends to overestimate the wave height by up to 0.5 m. It is also important to note the low number of HF radar data points. The HF radar data time series show just 35% data availability.

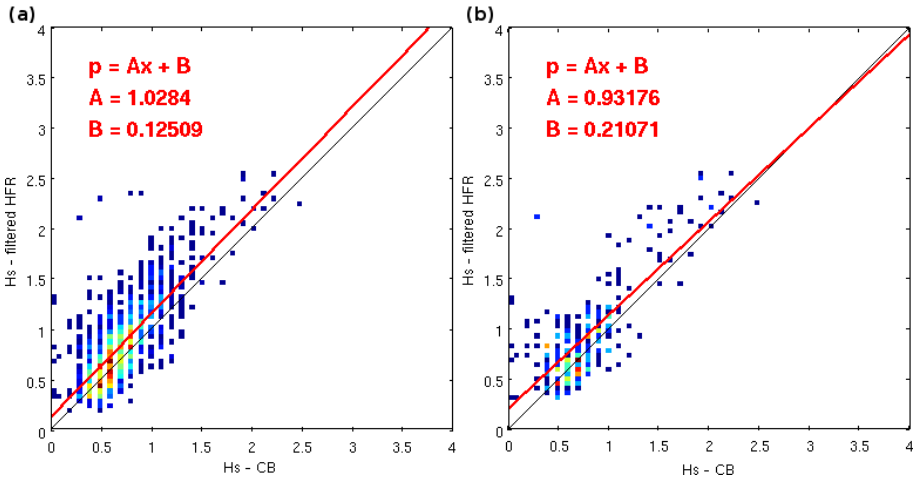

Figure 2. Scatter plots comparing the filtered HF radar data versus the Coastal Wave Buoy (CB) for two data periods. (**a**) The entire available data period (March–September 2014). (**b**) The study period (from 15 March to 15 May 2014).

2.3. Wind-Waves Spectral Description

The irregular nature of wind causes irregular wind-waves with different heights, periods and directions. For this reason, wind-waves are usually described using spectral techniques, where the random motion of the sea surface is treated as a summation of harmonic wave components. Specifically, the variance density spectrum $E(f,\theta)$ is used.

The normalized distribution of wave energy density over directions at one frequency is given by the directional distribution of the spectrum:

$$D(\theta,f) = \frac{E(f,\theta)}{E(f)} \tag{1}$$

From that, the directional spreading (DSPR) of the waves can be defined as the one-sided directional width of the spectrum:

$$DSPR^2 = \sigma_\theta^2(f) = \left(\frac{180}{\pi}\right)^2 \int_0^{2\pi} \left(2\sin\left(\frac{\theta-\overline{\theta}}{2}\right)\right)^2 D(\theta,f)d\theta \tag{2}$$

The SWAN model computes this quantity as conventionally for pitch-and-roll buoy data ([17]):

$$DSPR^2 = \left(\frac{180}{\pi}\right)^2 2\left(1-\sqrt{\left(\frac{\int \sin\theta E(\sigma,\theta)d\sigma d\theta}{\int E(\sigma,\theta)d\sigma d\theta}\right)^2 + \left(\frac{\int \cos\theta E(\sigma,\theta)d\sigma d\theta}{\int E(\sigma,\theta)d\sigma d\theta}\right)^2}\right) \tag{3}$$

Local wind-waves (sea system) show a broadband spectrum with a high variety of frequencies associated with irregular sea states. In contrast, waves generated far away (swell system) present a narrowband spectrum with a frequency range with little associated energy. It is well known that sometimes, different wave systems coexist, resulting in a mixed sea ([10]). Then, when the sea and swell components exist at the same time, bimodal spectra occur.

2.4. Numerical Model

The SWAN numerical model was used in this study. SWAN is a third-generation numerical wave model that computes random, short-crested waves in coastal regions with shallow water and ambient currents ([18]). It is based on the wave action balance Equation (4) with sources and sinks and incorporates the state-of-the-art formulations of the processes of wave generation, dissipation and wave-wave interactions (5).

$$\frac{\partial N}{\partial t} + \frac{\partial c_x N}{\partial x} + \frac{\partial c_y N}{\partial y} + \frac{\partial c_\sigma N}{\partial \sigma} + \frac{\partial c_\theta N}{\partial \theta} = \frac{S_{tot}}{\sigma} \tag{4}$$

$$S_{tot} = S_{in} + S_{nl3} + S_{nl4} + S_{ds,w} + S_{ds,b} + S_{ds,br} \tag{5}$$

The SWAN model has been previously used in the Catalan coast ([8,11,12]); thus, it has already been calibrated and validated, providing accurate results. In this study, the SWAN Model v40.91A is configured using the parametrization and coefficients established in the calibration undertaken by [11]. Non-stationary conditions, spherical coordinates and nautical convention have been selected. The wind growth is computed with a sum of a linear term and an exponential term. For the linear growth, the expression from [19] is used, and for the exponential growth, the expression and coefficients of [20] are used. The nonlinear quadruplet wave interactions are integrated by a fully-explicit computation of the nonlinear transfer with the Discrete Interaction Approximation (DIA; proposed by [21]) per sweep (using default coefficients). For the whitecapping, the [20] formulation is used with $C_{ds} = 2.36 \cdot 10^{-5}$, $\delta = 1$ and $p = 4$. Finally, the JONSWAP ([22]) bottom friction formulation is added with the default coefficients.

The spectrum is discretized with a constant relative frequency resolution of $\Delta f = 1.1$ (logarithmic distribution) and a constant directional resolution of $\Delta\theta = 10^\circ$. The discrete frequencies are defined between 0.01 Hz and 1 Hz. Above the high-frequency cutoff, a diagnostic tail f^{-4} is added. However, since buoys measure the integral parameters in a limited frequency range, the integral parameters H_s, T_p and wave direction have been calculated within the frequency range 0.03–0.6 Hz, in order to ensure that the modeled and measured quantities can be compared ([11]).

In order to generate the boundary conditions for the numerical model, a downscaling technique has been used. The entire system consists of three nested domains (see Figure 1). The largest one covers the western Mediterranean Sea with a spatial resolution of 15 km and provides boundary conditions to a second-level domain, which covers the Catalan Sea. This one has a spatial resolution of 3 km and provides boundary conditions to the local domain, which has a horizontal resolution of 350 m. This study is focused on this last domain.

The initial conditions have been obtained running the model in stationary mode. The bathymetry introduced in the model has a grid resolution of 0.0083° and was obtained from GEBCO (General Bathymetric Chart of the Oceans, www.gebco.net). Finally, for the wind forcing, outputs from the Weather Research and Forecasting (WRF; [23]) model run operationally at high resolution (3 km) at the Catalan Service of Meteorology (Servei Meteorològic de Catalunya (SMC)) are used.

2.5. Validation Techniques

In order to assess the model behavior, the estimation of the bias, the Root Mean Square Deviation (RMSD), the Pearson's correlation (Pearson's r) and the model skill score (d, following the method presented in [24]), is undertaken. These values are defined as follows:

$$bias = \frac{1}{N} \sum X_{model} - X_{obs} \tag{6}$$

$$RMSD = \sqrt{\frac{1}{N}\sum (X_{model} - X_{obs})^2} \quad (7)$$

$$r = \frac{\sum \left(\left(X_{model} - \overline{X_{model}} \right) \left(X_{obs} - \overline{X_{obs}} \right) \right)}{\sqrt{\sum \left(X_{model} - \overline{X_{model}} \right)^2} \sqrt{\sum \left(X_{obs} - \overline{X_{obs}} \right)^2}} \quad (8)$$

$$d = 1 - \frac{\sum |X_{model} - X_{obs}|^2}{\sum \left(|X_{model} - \overline{X_{obs}}| + |X_{obs} - \overline{X_{obs}}| \right)^2} \quad (9)$$

Pearson's r describes consistent proportional increases or decreases about respective means of the two quantities, but it makes too few distinctions among the type or magnitudes of possible covariations ([24]). By contrast, d is not a measure of correlation or association in the formal sense, but rather a measure of the degree to which a model's predictions are error free. Unlike r, d is sensitive to differences between the observed and predicted means, as well as to certain changes in proportionality ([24]). Note that analogously to r, d is measured from 0 to 1, 1 denoting maximum agreement.

3. Results

3.1. The Wind Field

In this sub-section, the quality of the wind input is analyzed (i.e., model versus measured wind data comparison) due to the high sensitivity of the modeled waves to the wind field ([10,25,26]). Figure 3 shows a comparison between the wind magnitude used to force the wave model and the wind measured by DB at 10 m above the sea surface. In general, good agreement is observed between both time series with a bias of -0.13 m/s, an RMSD of 1.82 m/s, an r of 0.83 and a d of 0.91. However, the orange boxes highlight three events where the wind magnitude is clearly underestimated, with biases greater than -1.7 m/s and RMSDs greater than 2 m/s. These events correspond to events with easterly winds. A plausible explanation for this underestimation of the easterly wind events is that the friction velocity parametrization of the operational atmospheric model run at the SMC was adjusted to work properly over the Catalan land area. Thus, when the wind comes from land (e.g., NW wind-jet events), it is properly modeled, but when the wind comes from the sea (e.g., easterly wind events), the friction velocity is too high, and therefore, the wind is too much decelerated. However, the easterly wind events are not the focus of this study. Thus, when ignoring these easterly wind events, the wind field shows good agreement with the buoy data. The selected wind-jet events are marked with green boxes in Figure 3, and their main characteristics are shown in Table 1. The table includes wind intensity calculated at P2, which is approximately located in the wind-jet axis, and some statistics comparing the WRF model data with DB. Note that DB is not located at the axis of the wind jet. The table shows that all of the events reaches maximum wind intensities above 16 m/s and have mean intensities above 9 m/s. E1 is the larger event and has less mean intensity because it is a two-peak storm, while the other events are single-peak storms. The statistics present an RMSD around 2 m/s, coinciding with the values usually obtained with the WRF operational model at the SMC, and the biases show good agreement, except for E2, where the model clearly overestimates the wind intensity compared with the buoy measurements.

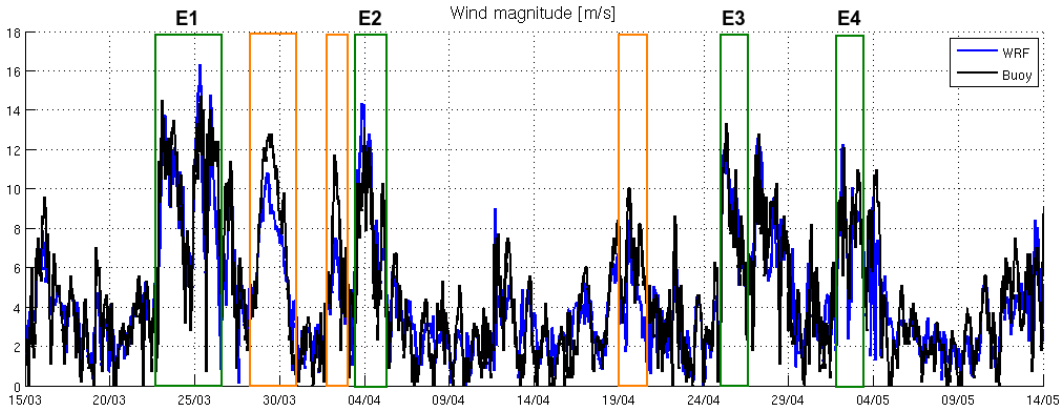

Figure 3. Wind magnitude measured at DB (black) compared with WRF model data (blue). The green boxes are the selected NW wind-jet events, and the orange boxes are the most underestimated wind events, which match easterly wind events. Time series data are for 2014.

Table 1. Main characteristics of the NW wind-jet events at point P2 according to WRF model results. Error metrics comparing DB data and WRF results are shown in terms of RMSD and bias.

Event	Period (dd/mm/yy)		Duration	Maximum Wind	Mean Wind	Bias	RMSD
	Start Day	End Day	(∼Days)	Intensity (m/s)	Intensity (m/s)	(m/s)	(m/s)
E1	22/03/14	27/03/14	4.5	16.70	9.43	−0.37	2.24
E2	03/04/14	04/04/14	1.5	16.62	11.27	1.65	2.31
E3	25/04/14	26/04/14	1	17.03	11.69	0.35	1.37
E4	02/05/14	03/05/14	1.5	16.62	10.87	−0.29	1.97

3.2. Numerical Model Skill Assessment

In order to validate the numerical model results, the modeled significant wave height (H_s), peak period (T_p) and nautical wave direction are compared with DB and CB observational data in Figures 4 and 5, respectively. It is important to note that the numerical model has been configured to measure these parameters within a similar frequency range as the buoys in order to be able to perform a reliable comparison. Nevertheless, it is worth noting that the H_s can be somewhat higher than in these time series, since the model and the buoys estimate H_s over a determined frequency range rather than over the entire frequency domain, as happens in nature. Figure 4 shows that, at the DB location, the SWAN model is able to capture the NW storm peaks fairly accurately during the four selected events. In all cases, the modeled H_s shows good agreement with the measurements. However, during E2, H_s shows faster decay, probably due to the sudden direction change measured by the buoy, which the model is not able to reproduce. In contrast, H_s is underestimated during the easterly storms, which is consistent with the aforementioned wind underestimation. The H_s during these events show a relative error around 50%.

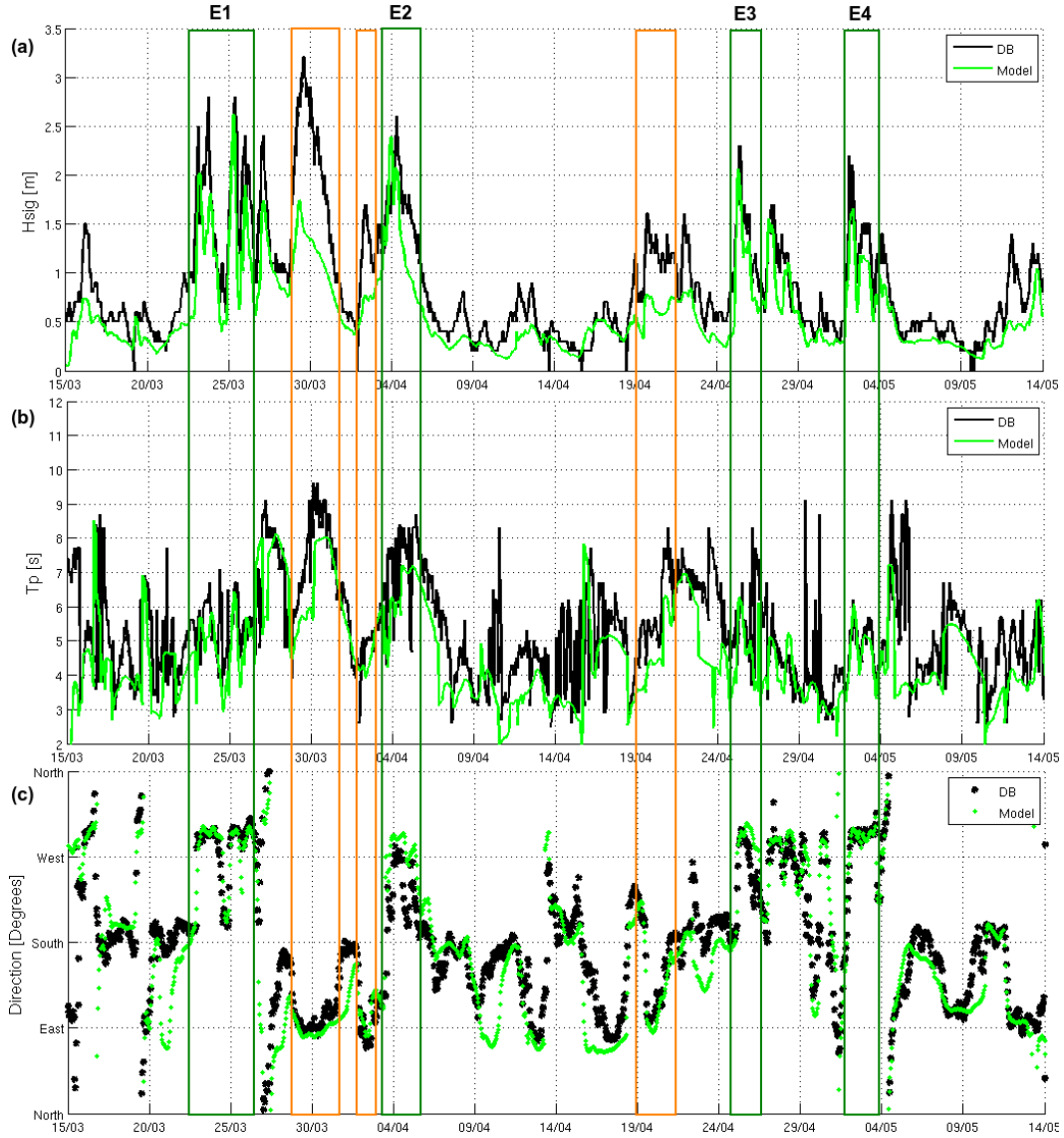

Figure 4. Comparison between model results (green) versus observed data at DB (black): (**a**) significant wave height, (**b**) peak period and (**c**) nautical direction. The green boxes are the selected wind-jet events, and the orange boxes are the most underestimated events, which match easterly wind events. Time series data are for 2014.

At CB (Figure 5), the three parameters (H_s, T_p and wave direction) show good agreement with the buoy data. In this case, the underestimation during the easterly storms is also present. However, in this case, the NW energetic events selected before do not have a relevant significant wave height. This is because the CB is located near the coast and out of the wind-jet axis, and thus, it is poorly affected by the NW storm. Figure 5 also includes the measurements from the HF radar. The third arc of the Salou antenna filtered HF radar data has been used in the comparison. Similarly to [27], the filter consists of removing the isolated data points, applying a median filter and eliminating the points where the change in wave height is over a threshold of 0.5 m. Even though the HF radar is able to capture the main pattern of significant wave height measured by the buoy, especially the storm peaks, it is important to note the low number of data points. In addition, as explained in Section 2.2, it can be observed that the shortest wave period included in the HF radar data is five seconds. Concerning the nautical direction, the HF radar data do not fit well with the buoy observations. This is reasonable since the buoy provides a point measurement, while the HF radar assumes that the ocean wave

spectrum is homogeneous throughout the range cell. Overall, the HF radar data are useful for a visual validation of the results of H_s and T_p, especially during a storm peak, but due to the scarcity of data, it is not possible to conduct a more thorough validation including a statistical analysis. The usefulness of the Ebro Delta HF radar wave data is further analyzed in Section 3.4.

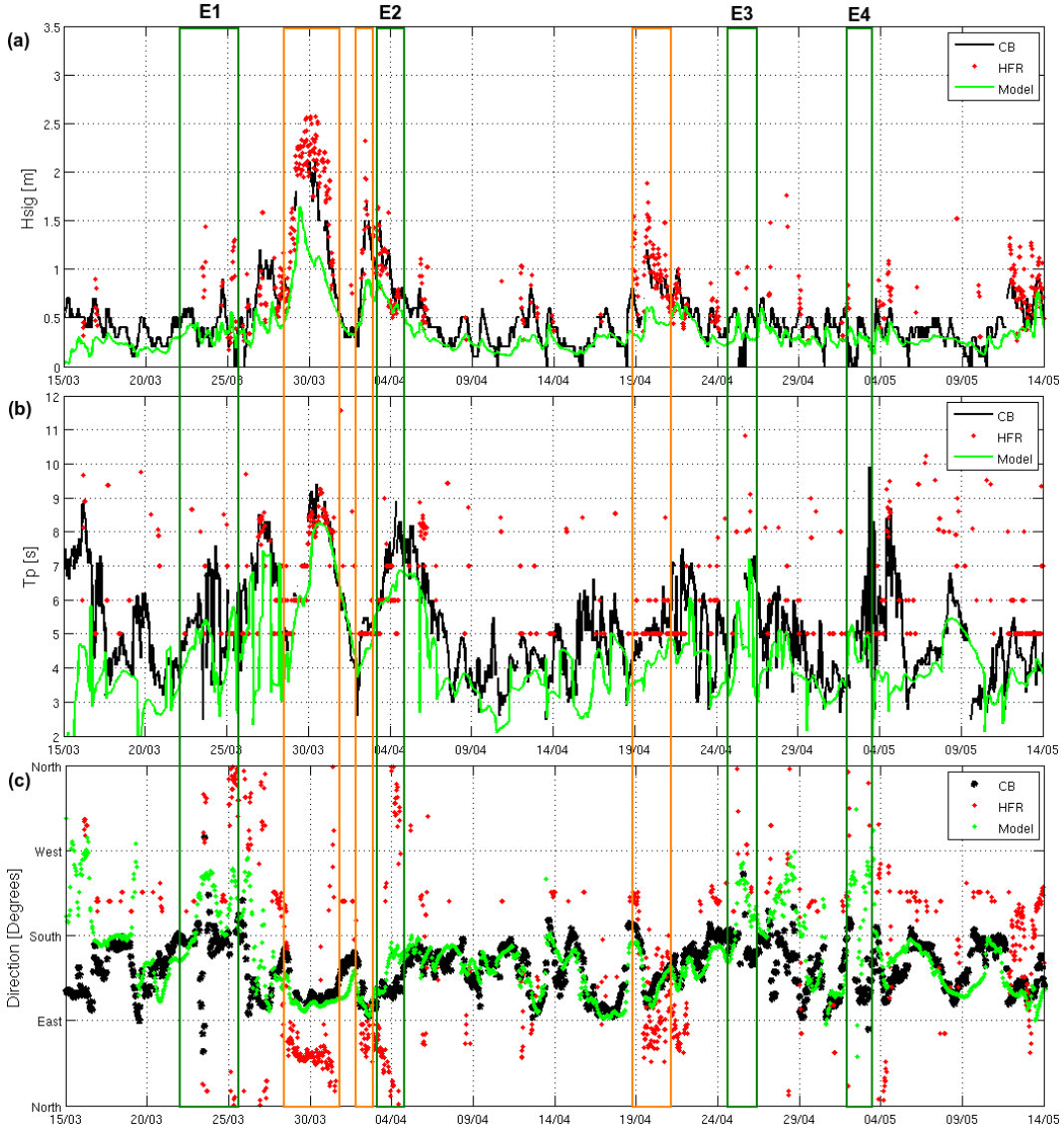

Figure 5. Model results (green) versus CB data (black) and HF radar data (red) comparison. (**a**) Significant wave height. (**b**) Peak period. (**c**) Nautical direction. The green boxes are the selected wind-jet events, and the orange boxes are the most underestimated events, which match easterly wind events. Time series data are for 2014.

The statistical analysis results comparing the model results with the measured data at the two buoys are shown in Table 2. The significant wave height shows biases around 0.2 m at the buoy sites and shows a better r and d at the DB location. The peak period present similar biases and RMSDs at both locations, but also presents a better agreement at the DB point. Finally, the mean wave direction exhibits a major variability and much higher agreement at DB than at CB. This is due to a larger variability of wave directions in an offshore position compared to a coastal position, where the directions tend to be more uniform due to the refraction phenomena in coastal areas (note that

the CB is moored at a 15-m water depth, while the DB is moored at a 688-m water depth). However, at the same time, this causes higher errors at CB than at DB intrinsically.

Table 2. Statistical comparison between the model results and DB and CB data of significant height (H_s), peak period (T_p) and mean direction (Dir), including bias, RMSD, r and d.

Parameter	Model Versus DB			Model Versus CB		
	H_s (m)	T_p (s)	Dir (°)	H_s (m)	T_p (s)	Dir (°)
Bias	−0.27	−0.76	−7.61	−0.17	−1.02	6.37
RMSD	0.39	1.46	42.03	0.24	1.66	29.03
r	0.89	0.62	0.87	0.86	0.49	0.49
d	0.86	0.75	0.92	0.77	0.65	0.71

Additional validation is carried out in terms of wave spectra because part of the investigation is based on the modeled spectrum. It is important to keep in mind that the SWAN model has been configured as a third-generation model, so it has no a priori restrictions on the evolution of the spectrum ([18]), i.e., the wave spectra are calculated integrating the energy balance equation. In Figure 6, the modeled spectrum (calculated between 0.01 and 1 Hz) is compared with the spectra measured at DB (which does not have a fixed frequency range) and CB (which measures between 0.03 and 0.66 Hz) in two time instants: 25 April 2014 at 06:00 UTC (during event E3; Figure 6a,b) and 3 May at 04:00 (during event E4; Figure 6c,d). Note the different frequency range of the two buoys and the different y scale. The spectrum at CB has much less energy than the spectrum at DB. This difference is also evident in Figures 4 and 5, where the wave height at CB for those events is around 0.5 m, while at DB, it exceeds 2 m. A first visual inspection shows that the modeled and measured spectra have a similar shape (unfortunately, the tail of the spectrum was not measured). At CB during E3 (Figure 6a), the modeled spectrum seems to be more bimodal than the measured spectrum, with more energy at higher frequencies. However, the amount of energy at this point is less than 0.04 m^2/Hz, which makes this difference not relevant, since it is a very coastal point. At the remaining spectra comparisons, the modeled and measured energy are similar except for a few frequency bands, which the numerical model underestimates. The spectra energy differences are consistent with the underestimation of the waves' parameters (e.g., see the negative biases for E3 in Table 2). Nevertheless, it is worth noting that buoy measurements are not error free and that buoys have problems measuring waves with short periods. Overall, the spectra obtained with the SWAN model are considered acceptable to be used as a tool to investigate the evolution of the wave response to a wind jet.

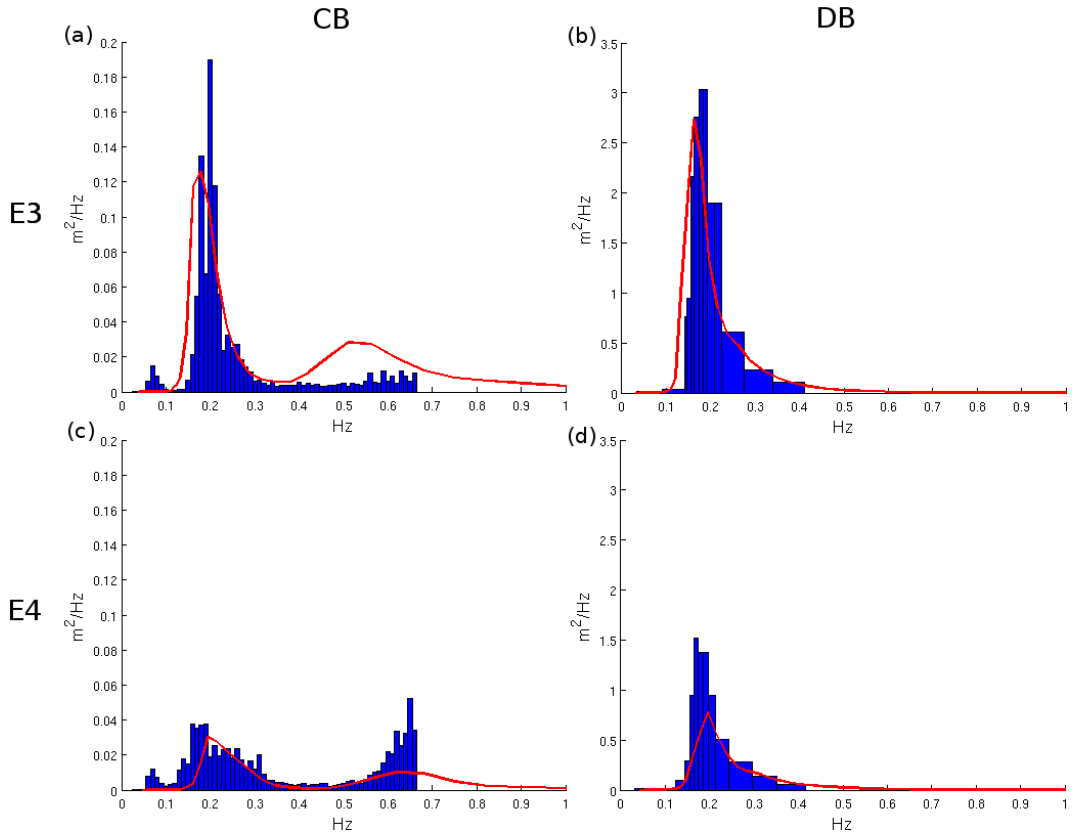

Figure 6. 1D wave spectra comparison between the model results (red line) and the spectra measured at DB and CB (blue histogram) at two time instants. (**a**) At CB within E3, (**b**) at DB within E4, (**c**) at CB within E4 and (**d**) at DB within E4. Note the different y scale for the two locations.

3.3. Wave Response to a NW Wind-Jet Event

From now on, in order to analyze the wind-jet evolution in time and in space, the numerical model results are used. The wave response during a wind-jet sequence is investigated in terms of the numerical wave spectra evolution. To do so, the event E3 has been selected. This wind-jet starts on 25 April at 02:00 and reaches its maximum intensity at 06:00. It is formed very quickly and fades gradually. Figure 7 shows the two-dimensional frequency-direction spectra evolution at the wind-jet axis (points P1 and P2) and out of it (point P3).

Before the wind-jet starts (Figure 7a), the wind intensity is small, and all three points show a mostly unimodal spectrum with the spectrum peak located in the south. When the wind jet starts (Figure 7b), the wave field is adapted to the new wind in less than one hour, and two different patterns are observed. At the wind-jet axis, P1 and P2 exhibit bimodal spectra, with a new peak in the wind direction (wind sea system). This peak reaches higher frequencies and is wider than the "old" one, indicating the irregularity of the waves. In contrast, at P3, the spectrum remains mostly unimodal, but it has been expanded to the W, as a result of the wind-jet influence. Then, when the wind-jet is intensified (Figure 7c), the spectral energy is also increased. In addition, since the wind jet becomes wider, the spectrum at P3 is more affected by it and, thus, exhibits a non-negligible energy increase. After the maximum wind intensity (Figure 7d), the spectral energy decreases. The remaining energy of the "old" peak is almost irrelevant, and a new peak is observed at the east, corresponding to a swell system. Finally, after 24 h (Figure 7e), a new sea system around the southern direction occurs jointly with the presence of the swell peak in the east and the remaining energy due to the wind jet in the NW (at point P2).

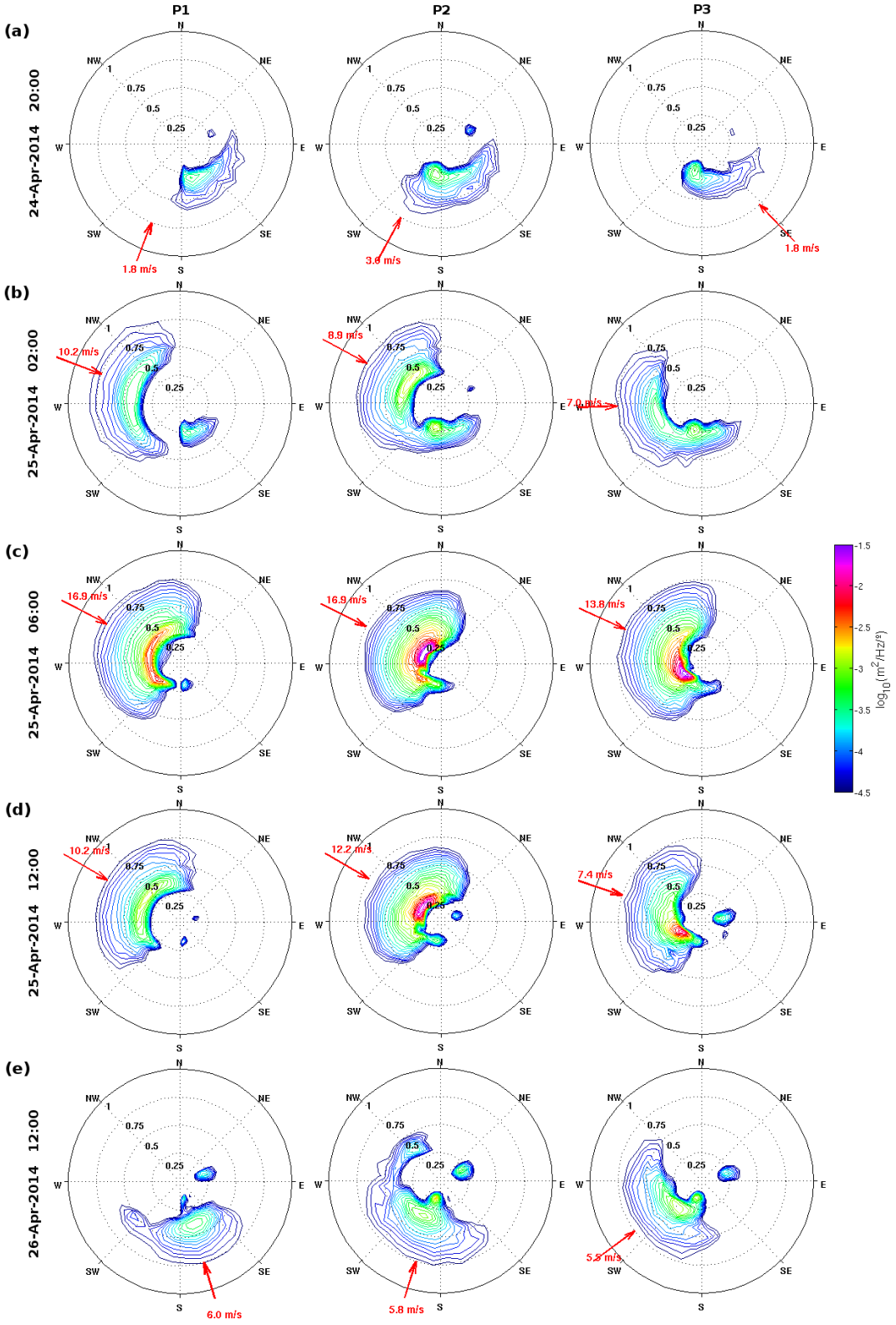

Figure 7. Evolution of the 2D variance density spectra during the wind-jet event E3 at P1 (first column), P2 (second column) and P3 (third column). Note that, in order to be able to compare the different spectra, the figure shows the logarithm of the variance density. The red arrows indicate the wind direction and intensity. Panels (**a**–**e**) show the time evolution.

Comparing the spectrum results in the analysis points (see Figure 1), more spectral energy is observed in P2 (offshore) in comparison to P1 (nearshore) due to a larger fetch. In addition, the energy peak in P2 is narrower than in P1 and P3, denoting a lower spreading. This leads one to consider the temporal evolution of the 2D maps in terms of wind intensity, significant wave height and directional spreading, as well as the evolution of these three variables along a section perpendicular to the wind jet (see Figure 8). At the start of the wind jet, the wave height and the directional spreading exhibit the clear influence of the wind: an increase of the wave height and a decrease of the spreading is observed at the wind-jet axis. Then, during the maximum intensity peak, the wind jet covers almost the entire domain. The wave height is much higher and the spreading is much less than before, also occupying roughly the entire domain. The inverse effect is observed when the wind jet is diminishing. Finally, at the end of the wind jet, the shape of the wind field distribution can be observed in the H_s and DSPR maps, which show the wind-jet axis clearly defined. In general, the evolution along the section presents a clear positive correlation between the wind intensity and the wave height and a negative correlation between the wind and the directional spreading. Thus, the directional spreading declines offshore-ward along the wind-jet axis and increases on either side of it.

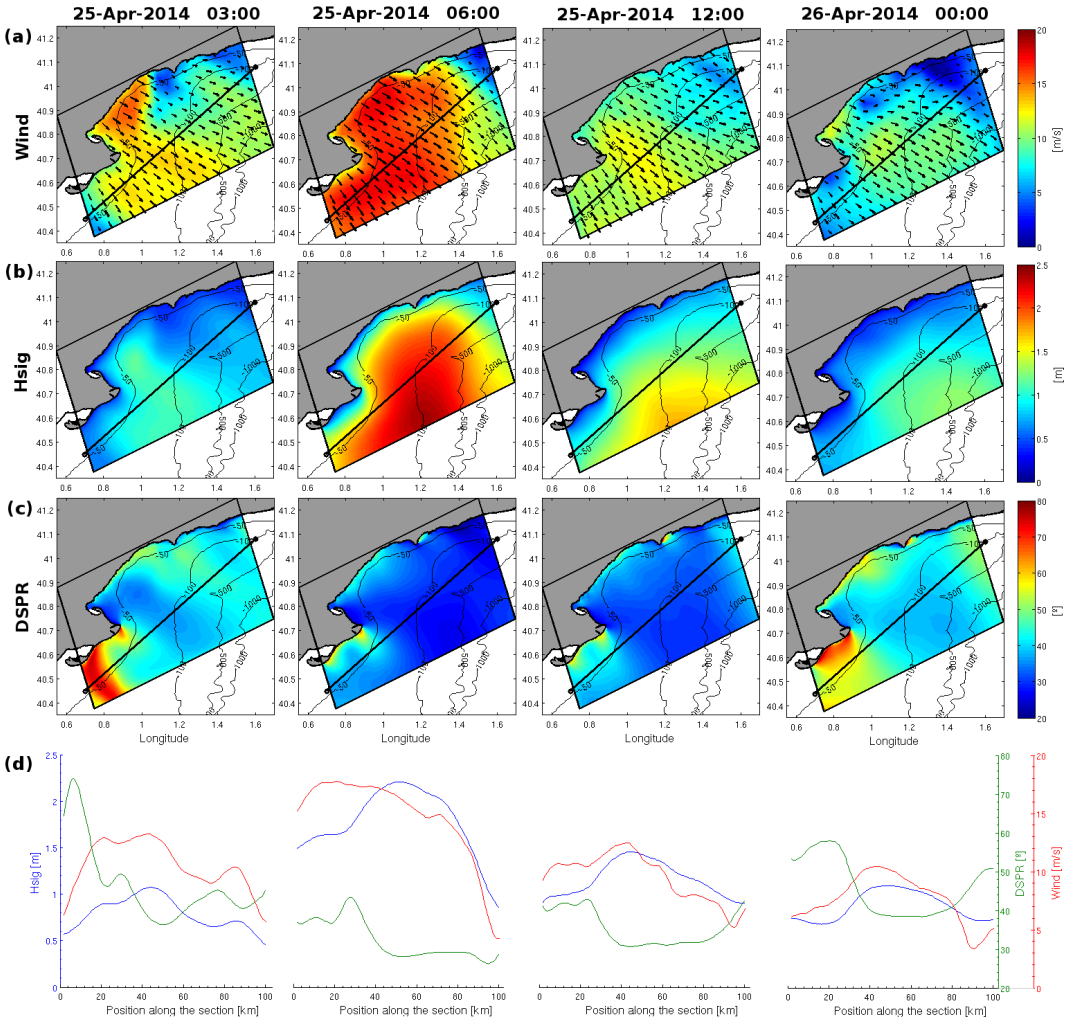

Figure 8. Model results for the wind-jet event E3. The figure shows the evolution of (**a**) the wind intensity, (**b**) the significant wave height, (**c**) the DSPR (directional spreading) and (**d**) the profile of the previous variables along the black line plotted in Panels (**a**–**c**).

So far, just the E3 event has been analyzed. In order to examine if the other three events develop in a similar way to E3, Figure 9 is analyzed. It presents the spectra at the start and the end of the wind

jet and the evolution of the wind intensity, significant wave height and directional spreading along a section at an instant within the events (analogously to Figure 7 and Figure 8 for E3). In all cases, multi-modal spectra occur at the beginning of the wind jet. At the end of it, a swell component at the east direction appears due to the northerly winds developed at the northern part of the coast. The behavior observed along the sections is the same as shown above for E3. The wave height follows the wind pattern, and the directional spreading is negatively correlated with the wind intensity.

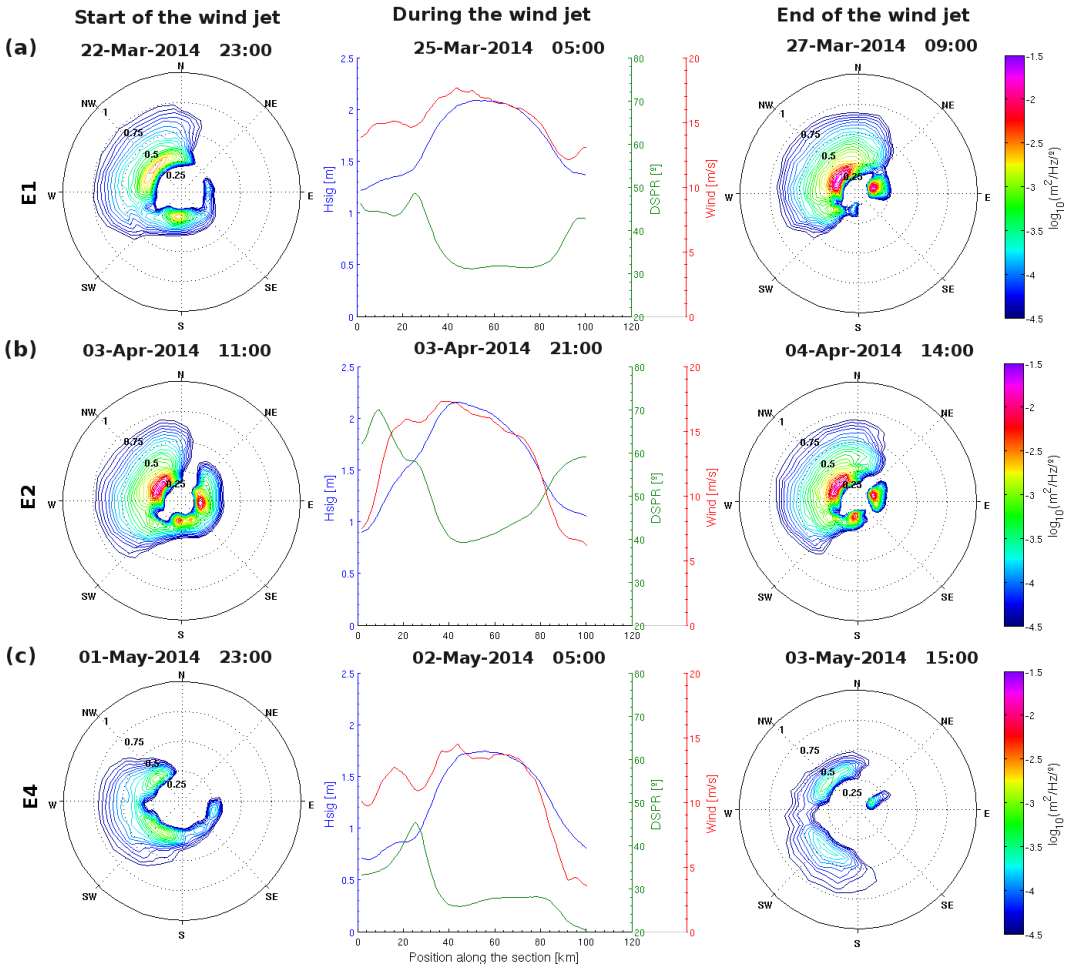

Figure 9. Wind jet responses for the remaining events. The spectrum at P2 at the start and the end of the wind jet is presented, as well as a section of the behavior during the wind jet. (**a**) Event E1. (**b**) Event E2. (**c**) Event E4.

3.4. Reliability of the Ebro Delta HF Radar Wave Data

In order to investigate the reliability of the HF radar data, first its raw data are examined. In Figure 10, the HF radar raw data are compared with the measured data by CB. There is a relevant data dispersion, many isolated data points and points with unrealistic measurements that reach values up to 16 m. For these reasons, HF radar data must be cautiously post-processed in order to be able to use it properly.

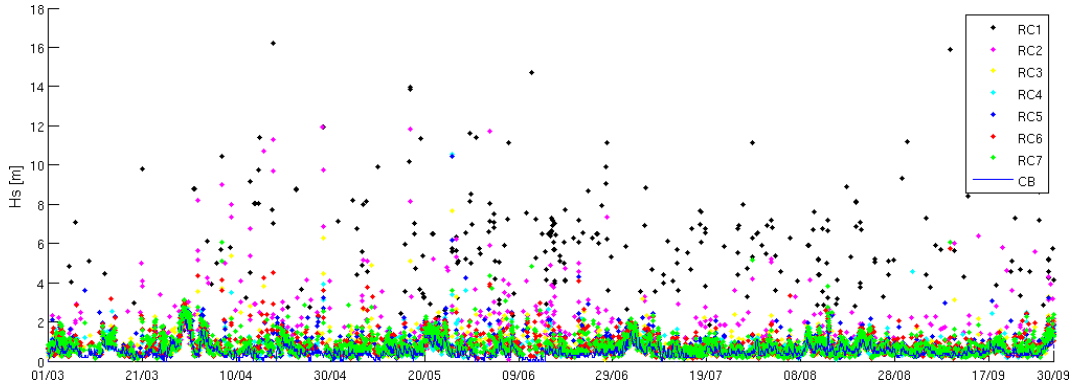

Figure 10. HF radar data of the Salou antenna for all of the Range Cells (RCs) compared with the CB measured data. Time series data are for 2014.

In Section 3.2, the HF radar data of the Salou antenna have been compared with the CB measurements and the model results. As explained earlier, the comparison was carried out by applying a median filter and considering a threshold in a similar way as [27]. In their study, [27] performed direct comparisons between median-filtered wave height and period data from SeaSonde sites and the closest in situ wave buoy. They removed the SeaSonde points where the data were not available and the points exceeding a 1-m threshold change in less than an hour.

In a more recent study, [28] implemented a selection methodology to identify the proper HF radar range cells to be compared with a Waverider buoy. In order to use CODAR data to perform wave characteristic studies, [28] selected the useful data considering the percentage of captured data and the percentage of existing outliers. The work in [28] found that the dispersion of measured data across the selected Range Cells (RCs) was small, which permitted CODAR-buoy comparison by means of average values of useful data from all of the selected RCs.

In order to evaluate the reliability of the Ebro Delta HF radar, the method followed by [28] is implemented. The Salou antenna is first considered. To start, the differences in H_s between the RCs are calculated. The results show that the differences in RC1 and RC2 are significant in comparison with the other RCs. Then, the outliers presented in [28] are applied to the HF radar data comparing it with the CB data. Figure 11 shows the overview of useful data for each RC based on: (a) 25% outliers, (b) 50% outliers and (c) 75% outliers. It can be seen that 75% outliers presents more useful data, followed by 50% outliers and, finally, 25% outliers. In addition, the calculation of r for each RC (excluding RC1 and RC2) gives values in the range of 0.87–0.96, 0.89–0.91 and 0.95–0.96 for 75%, 50% and 25% outliers, respectively.

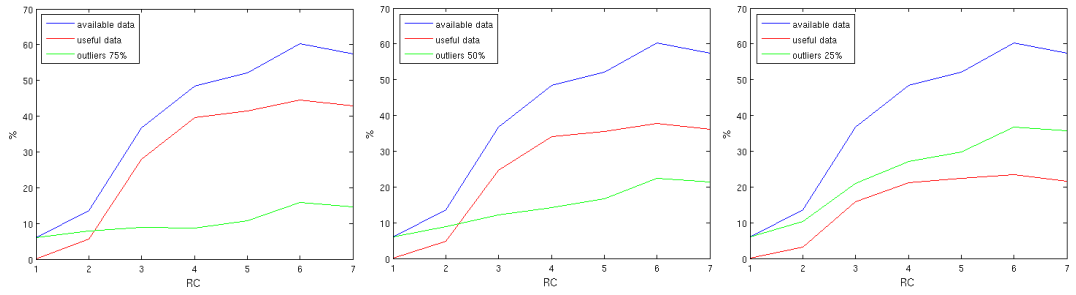

Figure 11. Percentage of available data (blue), outliers (green) and resulting useful data (red) for each range cell. (**a**) Applying 25% outliers. (**b**) Applying 50% outliers. (**c**) Applying 75% outliers.

Considering all of these results, RCs from 3–7, and 50% outliers have been selected as the most appropriate to be applied, since 75% outliers, although containing more useful data, presents lower

values of correlation (similar to [28]). Now, taking a mean of the RCs from 3–7, the results presented in Figure 12 are obtained. The figure compares the mean of the selected HF radar data RCs with the measurements of CB. The results show a good agreement between the two datasets, with a bias of 0.06 m, RMSD of 0.11 m, an r of 0.92 and a d of 0.95. Therefore, it can be said that the HF radar is able to follow the same tendency as the measured data. However, as in Section 3.2, it is worth noting the scarcity of HF radar data points (only around 30%–40% is useful data). Since the HF radar does not measure waves with periods lower than 5 s, a plausible explanation for the scarcity of data is that most periods at the Catalan coast are between 2 s and 4 s ([1]). This, added to the intrinsic loss of measured data of the HF radar, could be the cause for such few data points.

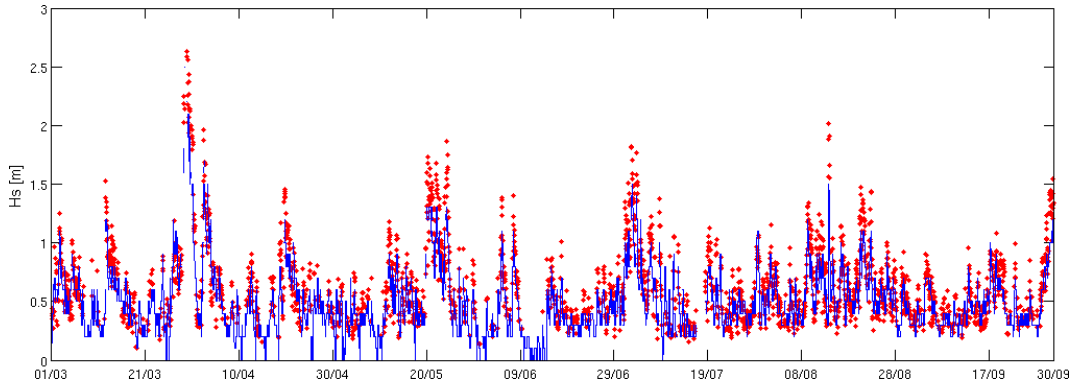

Figure 12. Time series comparison between the measured data at CB (blue) and the averaged HF radar data at range cells from 3–7 selected by applying 50% outliers. Time series data are for 2014.

When implementing the same method in the Alfacada antenna, a substantial problem appears: there is no alternative measurement to apply outliers. As [28] pointed out, a simultaneous set of data from an alternative source (e.g., a buoy) is needed to apply their radar noise filter. For this reason, the authors attempted a method using concepts from both [27] and [28]. First, the H_s differences between the RCs were computed, and as with the Salou antenna, RCs 3–7 were selected. Then, similar to Section 3.2, a median filter and a 0.5-m threshold filter were applied. In this case, the resulting percentage of useful data (see Figure 13) is higher than before, since there is also more available data than in the Salou antenna.

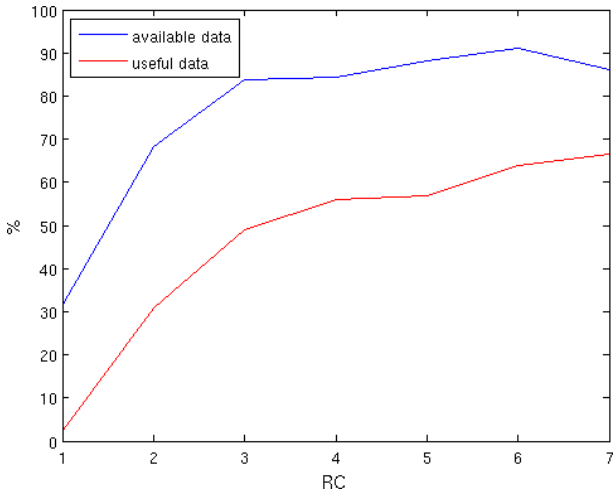

Figure 13. Percentage of HF radar data availability (blue) and useful data after applying the filter (red) for each RC.

Lastly, the mean of the resulting filtered data for RCs 3–7 was taken. The final processed HF radar data are presented in Figure 14. There are still some isolated unrealistic points, but the data are sufficiently treated to be useful to see the wave height tendency. However, although there are more data points than at the Salou antenna, the scarcity of data remains visible.

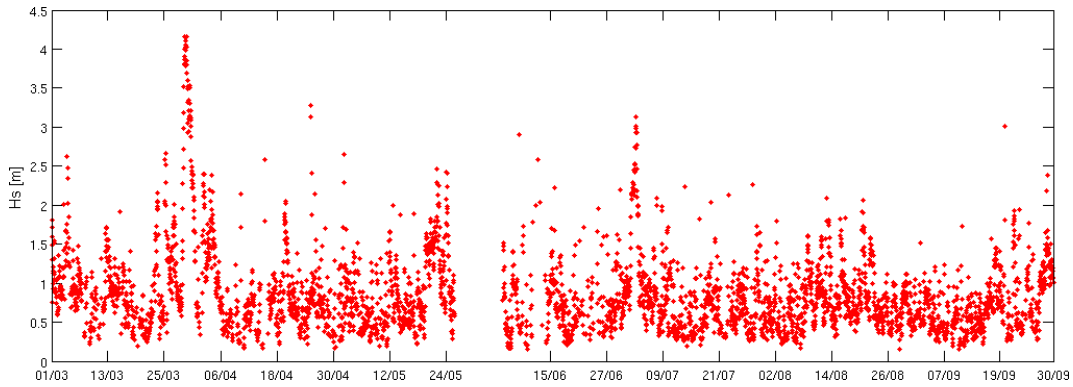

Figure 14. Treated HF radar data of the Alfacada antenna. Time series data are for dd/mm/2014.

4. Discussion

The synoptic situation that causes the NW wind jets at the Ebro Delta is analyzed. During the NW wind-jet event E3, a high-pressure system over the Iberian Peninsula and a low-pressure system situated in front of the Catalan coast occurred (see Figure 15). The synoptic situation during E1 is similar to E3, but with a wider low-pressure area with higher gradients, covering the entire NW Mediterranean. For event E2, the circumstances are almost the same as in E3, and during E4, the synoptic situation presents a high-pressure system at the Bay of Biscay and a low-pressure system centered at the Ligurian Sea. These results are consistent with previous studies. For instance, [14] described the synoptical patterns of the mistral. They noted that when the Iberian Peninsula is affected by the southeast flank of an anticyclone, with the isobars entering through the Pyrenees from the NE, a pressure gradient is established in the Ebro Valley from NW to SE, generating a mistral wind. In addition, [14] affirmed that it becomes stronger when cyclogenesis develops in the western Mediterranean (Gulf of Lion) or when a low persists in that area.

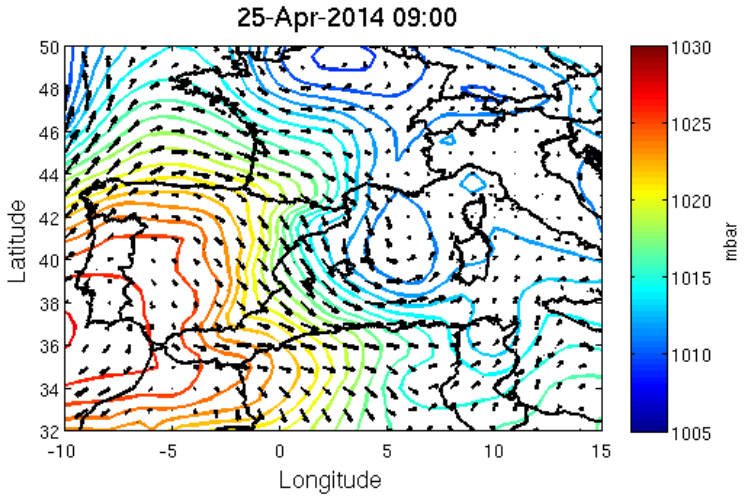

Figure 15. Synoptic situation on 25 April at 09:00 (i.e., during E3). This figure was created with data from the ECMWF reanalysis (http://www.ecmwf.int). The black arrows are the wind field at 10 m above the sea surface, and the contour plot corresponds to the sea level pressure.

All of these synoptic situations develop northerly winds at the north of the Catalan coast together with NW winds at the Ebro Delta region. The wind and wave pattern results from the second-level domain during E3 are presented in Figure 16. The coexistence of N and NW winds is observed, which induces a bimodal spectrum at the Ebro Delta (observed before in Figure 7d). Apart from the NW wind at the Ebro Delta, associated with the wind-sea system, there is an intense northerly wind at the northern part of the coast that generates waves propagating to the south, but due to the diffraction phenomena, these waves are likely rotated to the east and can be observed at the Ebro Delta as a swell system.

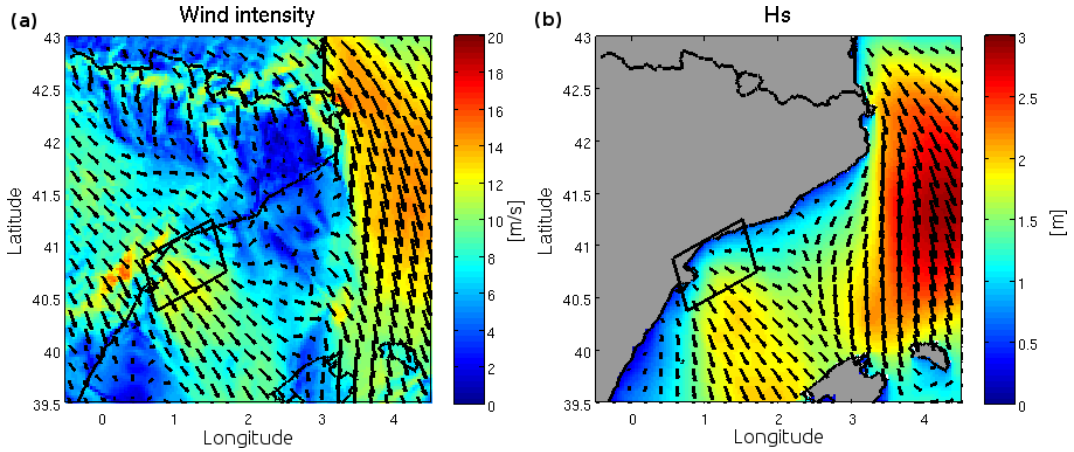

Figure 16. Results of the second-level domain on 25 April at 12:00. (**a**) Wind intensity. (**b**) Significant wave height and wave direction. The black rectangle corresponds to the local domain.

Overall, the four NW wind-jet events reported in the study period were created in similar synoptic situations. Thus, one can state that it is a frequent occurrence. For this reason, it is important to have numerical models able to forecast these events at the Ebro Delta, where a bimodal situation occurs due to the coexistence of N and NW winds.

The results described here show that a bimodal spectrum occurs at the start and the end of a wind jet and that the energy peak has more energy offshore than nearshore. Similar results were obtained by [2], who found that, in wind-jet regions, the spectra show one primary peak whose direction coincides with the local wind direction and that with increasing offshore distance, the peak energy increases and the peak frequency downshifts. The work in [2] also found that the overall directional spreading corresponds to the wind intensity distribution. They said that it is negatively correlated with wind energy and is small in wind-jet regions (<40°) and large at wake regions (>40°). In the present study, similar values are observed. At the wind-jet axis, the directional spreading is less than 40°, and it is higher when the measurement point is located out of the wind-jet axis and when the measurement is taken before the wind jet starts. The section evolution plots in Figures 8 and 9 show that the wave height is positively correlated with the wind intensity, but considering the y scale difference between the two magnitudes, it is observed that the wind intensity increases more than the wave height. This is consistent with [2], who stated that the significant wave height fluctuations coincided with wind energy variations, but whose intensities were much smaller than those of wind energy.

Regarding the wave response to the wind turn, the results obtained at the Ebro Delta show a clear bimodal spectrum for a wind turn of the order of 90°. For instance, in Figure 7a,b, it can be observed that a wind turn from SSW to WNW is able to develop a bimodal spectrum. This behavior is similar to the one observed by [29], who performed several numerical experiments with third-generation wave models and found that for wind shifts of 90° and greater, the coupling between the old sea and the newly-generated wind waves became sufficiently weak that the wave-wave interactions were unable to suppress the development of a new high-frequency wind-sea peak in the new wind direction.

Thus, a second, independent wind-sea spectrum was generated in the new wind direction, while the old wind-sea gradually decayed as swell. In contrast, [7] found that a 180° wind turn developed a bimodal spectrum, but for a 90° wind turn, the spectrum remained unimodal and only changed to a new direction.

The analysis of the HF radar data reliability performed in Section 3.4 shows that, due to its scarcity of data, the HF radar data can be useful for undertaking climatology, where the wave height tendency could be enough, but it is not useful for studying a specific event. For instance, in Figure 17, the comparison between the resulting processed HF radar data at the Alfacada site and the modeled wave height at different locations within the Alfacada antenna range during the event E3 is presented. The authors note that the HF radar data are not useful for validating a short specific event. In addition, it is worth noting the differences between the modeled time series. These differences cannot be seen by the HF radar, because HF radar data represent averaged measurements over RCs of some kilometers in size and, thus, cannot measure individual waves or differentiate different behavior along an RC. In this sense, it is important to note that [27] found good agreement between the two datasets, but also stated that, in their study area, the wave height is only minimally variable from 3–45 km off the coast.

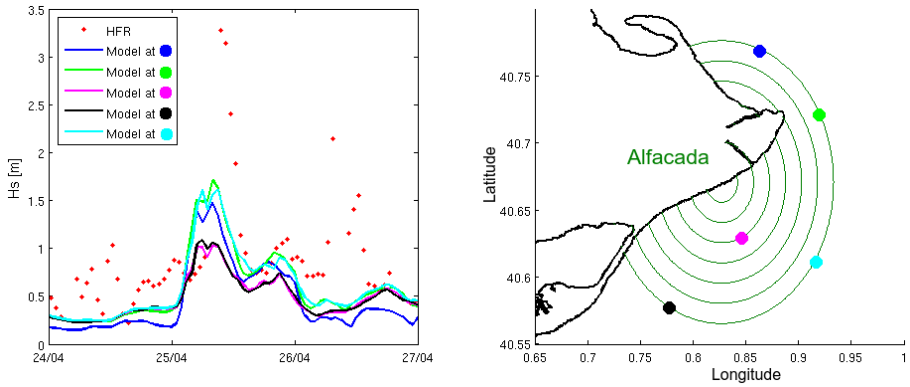

Figure 17. Treated HF radar data of the Alfacada antenna compared with different modeled time series from points located within the antenna range. Time series data are for 2014.

Since for young wind sea, most of the stress in the boundary layer is determined by momentum transfer from wind to waves ([30]), an important future work to be considered could be the wave and atmosphere model coupling in order to parametrize the sea-surface roughness properly. As a matter of fact, [31] stated that the modification of the wind drag coefficient by waves appeared to be the most crucial element, especially in regions where the wind-induced dynamics have a predominant role. Another thing to consider is the implementation of sea-swell partitioning, which is now available in an updated SWAN release (end of July 2016). In this new version, the model includes wave spectral partitioning based on the watershed algorithm of [32]. The first partition is due to wind sea, and the remaining partitions are the swell. Finally, working with the new Sentinels data could be a good way to overcome the scarcity of measured wave data in the region.

5. Conclusions

The SWAN numerical model has been implemented at the Ebro Delta, presenting good agreement with observational data. Within the study period (two months), four wind-jet events were selected to investigate the wind-wave response in terms of wave spectra, significant wave height and directional spreading. According to the model results, the wave field exhibits a noteworthy spatial and temporal variability. The significant wave height presents a positive correlation with the wind intensity and shows a spatial distribution in accordance with the wind field. In contrast, the wave directional spreading presents a negative correlation with the wind intensity, resulting in a lower

wave dispersion at the wind-jet axis. There is also differences of wave directional spreading along the wind-jet axis, being higher in the nearshore zone. The model results of wave spectra show a bimodal spectrum at the start and the end of the wind jet, when a wind-sea system and a swell system coexist, and a unimodal spectrum (due to a wind-sea system) during the wind jet, with the wave direction matching with the wind direction. Bimodal spectra are very common in the region due to the synoptic conditions that induce the NW wind jets. These are usually accompanied by northerly winds at the north of the Catalan coast, which produce the swell system at the Ebro Delta.

It is worth noting that this is the first time that the spectral evolution at the Ebro Delta has been analyzed in time and space, and thus, future research including more measured data (e.g., the new Sentinels) should be considered.

Finally, the reliability of the Ebro Delta HF radar data has been also investigated. HF radar raw data cannot be used directly; they must be post-processed. In this study, different methods have been used to filter the HF raw data, and the results show that the quality of the treated HF radar data is rather good. Thus, it is a data source that must be considered in future studies. However, the HF radar time series are full of gaps and are not useful for studying the evolution of a short-duration specific event. Additionally, when using HF radar wave data, it is important to remember that HF radar samples are homogeneous along a range cell, and thus, they give an average of the wave parameters over areas of the size of the range cell range, but cannot see individual waves. Therefore, it is important to consider the wave variability of the region. If it is quite homogeneous, the HF radar data could be more representative of real conditions, but, if the region presents big wave gradients, the HF radar data could be measuring something very different than the typical buoy data to which the authors are accustomed.

Acknowledgments: The development of this research is funded by the Doctorats Industrials 2013 PhD program (2013 DI 043) of the Catalan Government and partially supported by the project PLAN-WAVE (CTM2013-45141-R). The first author thanks the UPC (Universitat Politècnica de Catalunya) and the SMC (Servei Meteorològic de Catalunya) for their support and contribution. The authors also acknowledge Puertos del Estado for the dataset provided and Qualitas instruments for their support in the HF radar data analysis. This work has received funding from the UE H2020 program under grand agreement No. 730030 (CEASLESS project).

Author Contributions: Laura Ràfols, Elena Pallares, Manuel Espino and Manel Grifoll conceived of and designed the experiments. Laura Ràfols performed the experiments, analyzed the data and wrote the paper. Manel Bravo analyzed the wind data. Agustín Sánchez-Arcilla contributed analysis ideas. Abdel Sairouní contributed material. All of the authors contributed ideas in the writing process.

Conflicts of Interest: The authors declare no conflict of interest. The founding sponsors had no role in the design of the study; in the collection, analyses or interpretation of data; in the writing of the manuscript; nor in the decision to publish the results.

References

1. Bolaños, R.; Jorda, G.; Cateura, J.; Lopez, J.; Puigdefabregas, J.; Gomez, J.; Espino, M. The XIOM: 20 years of a regional coastal observatory in the Spanish Catalan coast. *J. Mar. Syst.* **2009**, *77*, 237–260.
2. Shimada, T.; Kawamura, H. Wind-wave developement under alternating wind jets and wakes induced by orographic effects. *Geophys. Res. Lett.* **2006**, *33*.
3. Ralston, D.; Jiang, H.; Farrar, T. Waves in the Red Sea: Response to monsoonal and mountain gap winds. *Cont. Shelf. Res.* **2013**, *65*, 1–13.
4. Wyatt, L. The effect of fetch on the directional spectrum of Celtic Sea storm waves. *J. Phys. Oceanogr.* **1994**, *25*, 1550–1559.
5. Laface, V.; Arena, F.; Guedes-Soares, C. Directional analysis of sea storms. *Ocean Eng.* **2015**, *107*, 45–53.
6. Zhou, L.; Wang, A.; Guo, P. Numerical simulation of sea surface directional wave spectra under typhoon wind forcing. *J. Hydrodyn.* **2008**, *20*, 776–783.
7. Aijaz, S.; Rogers, W.; Babanin, A. Wave response to sudden changes in wind direction in finite-depth waters. *Ocean Mod.* **2016**, *103*, 98–177.
8. Alomar, M.; Sánchez-Arcilla, A.; Bolaños, R.; Sairouni, A. Wave growth and forecasting in variable, semi-enclosed domains. *Cont. Shelf Res.* **2014**, *87*, 28–40.

9. Grifoll, M.; Navarro, J.; Pallares, E.; Ràfols, L.; Espino, M.; Palomares, A. Ocean-atmosphere-wave characterisation of a wind jet (Ebro shelf, NW Mediterranean Sea). *Nonlinear Proc. Geoph.* **2016**, *23*, 143–158.
10. Sánchez-Arcilla, A.; González-Marco, D.; Bolaños, R. A review of wave climate and prediction along the Spanish Mediterranean coast. *Nat. Hazards Earth Syst. Sci.* **2008**, *8*, 1217–1228.
11. Pallares, E.; Sánchez-Arcilla, A.; Espino, M. Wave energy balance in wave models (SWAN) for semi-enclosed domains—Application to the Catalan coast. *Cont. Shelf Res.* **2014**, *87*, 41–53.
12. Bolaños-Sanchez, R.; Sánchez-Arcilla, A.; Cateura, J. Evaluation of two atmospheric models for wind-wave modelling in the NW Mediterranean. *J. Mar. Syst.* **2007**, *65*, 336–353.
13. Grifoll, M.; Aretxabaleta, A.; Espino, M. Shelf response to intense offshore wind. *J. Geophys. Res. Oceans* **2015**, *120*, 6564–6580.
14. Riosalido, R.; Vázquez, L.; Gorgo, A.; Jansà, A. Cierzo: Northwesterly wind along the Ebro Valley as a meso-scale effect induced on the lee of the Pyrenees mountain range: A case study during ALPEX Special Observing Period. *Sci. Results Alp. Exp. (ALPEX)* **1986**, *2*, 565–575.
15. Lipa, B.; Nyden, B. Directional Wave Information From the SeaSonde. *IEEE J. Ocean Eng.* **2005**, *30*, 221–231.
16. Kohut, J.; Roarty, H.; Licthenwalner, S.; Glenn, S.; Barrick, D.; Lipa, B.; Allen, A. Surface current and wave validation of a nested regional HF radar Network in the Mid-Atlantic Bight. In Proceedings of the 2008 IEEE/OES 9th Working Conference on Current Measurement Technology (CMTC), Charleston, SC, USA, 17–19 March 2008.
17. Kuik, A.; van Vledder, G.; Holthuijsen, L. A Method for the Routine Analysis of Pitch-and-Roll Buoy Wave Data. *J. Phys. Oceanogr.* **1988**, *18*, 1020–1034.
18. Booij, N.; Ris, R.; Holthuijsen, L. A third-generation wave model for coastal regions-1. Model description and validation. *J. Geophys. Res.* **1999**, *104*, 7649–7666.
19. Cavaleri, L.; Malanotte-Rizzoli, P. Wind wave prediction in shallow water: Theory and applications. *J. Geophys. Res.* **1981**, *86*, 961–973.
20. Komen, G.; Hasselmann, S.; Hasselmann, K. On the existence of a fully developed wind-sea spectrum. *J. Phys. Oceanogr.* **1984**, *14*, 1271–1285.
21. Hasselmann, S.; Hasselmann, K.; Allender, J.; Branett, T. Computations and parameterizations of the nonlinear energy transfer in a gravity wave spectrum. Part II: Parameterizations of the nonlinear transfer for application in wave models. *J. Phys. Oceanogr.* **1985**, *15*, 1378–1391.
22. Hasselmann, K.; Barnett, T.; Bouws, E.; Carlson, H.; Cartwright, D.; Enke, K.; Ewing, J.; Gienapp, H.; Hasselmann, D.; Kruseman, P.; et al. *Measurements of Wind-wave Growth and Swell Decay During The Joint North Sea Wave Project (JONSWAP)*; Technical Report 12; Deutches Hydrographisches Institut; Hamburg, Germany, 1973.
23. Skamarock, W.; Klemp, J.; Dudhia, J.; Gill, D.; Barker, D.; Duda, M.; Huang, X.; Wang, W.; Powers, J. *A Description of the Advanceed Research WRF, Version 3*; NCAR Technical Note; National Center for Atmospheric Research: Boulder, CO, USA, 2008.
24. Willmott, C. On the validation of models. *Phys. Geogr.* **1981**, *2*, 184–194.
25. Cavaleri, L.; Bretotti, L. Accuracy of the modelled wind and wave fields in enclosed seas. *Tellus* **2004**, *56A*, 167–175.
26. Ponce de León, S.; Guedes Soares, C. Sensitivity of wave model predictions to wind fields in the Western Mediterranean sea. *Coast. Eng.* **2008**, *55*, 902–929.
27. Long, R.; Barrick, D.; Largier, J.; Garfield, N. Wave Observations from Central California: SeaSonde Systems and In Situ Wave Buoys. *J. Sensors* **2011**, *2011*, 728936.
28. Atan, R.; Goggins, J.; Harnett, M.; Agostinho, P. Assessment of wave characteristics and resource variability at a 1/4-scale wave energy test site in Galway Bay using waverider and high frequency radar (CODAR) data. *Ocean Eng.* **2016**, *117*, 272–291.
29. Young, I.; Hasselmann, S.; Hasselmann, K. Computations of a Wave Spectrum to a Sudden Change in Wind Direction. *J. Phys. Oceanogr.* **1987**, *17*, 1317–1338.
30. Janssen, P. Quasi-linear theory of wind generation applied to wave forecasting. *J. Phys. Oceanogr.* **1991**, *21*, 1631–1642.

31. Jorda, G.; Bolaños, R.; Espino, M.; Sánchez-Arcilla, A. Assessment of the importance of the current-wave coupling in the shelf ocean forecasts. *Ocean Sci.* **2007**, *3*, 345–362.
32. Hanson, J.; Phillips, O. Automated Analysis of Ocean Surface Directional Wave Spectra. *J. Atmos. Ocean. Technol.* **2001**, *18*, 277–293.